Photobiocidal-triboelectric nanolayer coating of photosensitizer/silica-alumina for reusable and visible-light-driven antibacterial/antiviral air filters

Sang Bin Jeong [a,b,1], Dong Uk Lee [c,d,1], Byeong Jin Lee [d,e], Ki Joon Heo [f], Dong Won Kim [g], Gi Byoung Hwang [f], Alexander J. MacRobert [h], Jae Hak Shin [a], Hyun Sik Ko [a], Se Kye Park [d,i], Yong Suk Oh [j], See Jo Kim [e], Dong Yun Lee [i], Seung-Bok Lee [b], Inyong Park [k], Sang Bok Kim [k], Bangwoo Han [k], Jae Hee Jung [a,*], Dong Yun Choi [d,*]

[a] Department of Mechanical Engineering, Sejong University, Seoul 05006, Republic of Korea
[b] Center for Environment, Health and Welfare Research, Korea Institute of Science and Technology, Seoul 02792, Republic of Korea
[c] Department of Industrial Chemistry, Pukyong National University, Busan 48513, Republic of Korea
[d] Biomedical Manufacturing Technology Center, Korea Institute of Industrial Technology, Yeongcheon 38822, Republic of Korea
[e] School of Mechanical Engineering, Andong National University, Andong 36729, Republic of Korea
[f] Material Chemistry Research Centre, Department of Chemistry, University College London, London WC1H 0AJ, United Kingdom
[g] Research Institute for Green Energy Convergence Technology, Gyeongsang National University, Jinju 52828, Republic of Korea
[h] UCL Division of Surgery and Interventional Science, Royal Free Campus, London NW3 2PF, United Kingdom
[i] Department of Polymer Science and Engineering, Kyungpook National University, Daegu 41566, Republic of Korea
[j] Department of Mechanical Engineering, Korea Advanced Institute of Science and Technology, Daejeon 34141, Republic of Korea
[k] Department of Environmental Machinery, Korea Institute of Machinery and Materials, Daejeon 34103, Republic of Korea

ABSTRACT

Outbreaks of airborne pathogens pose a major threat to public health. Here we present a single-step nanocoating process to endow commercial face mask filters with photobiocidal activity, triboelectric filtration capability, and washability. These functions were successfully achieved with a composite nanolayer of silica-alumina (Si-Al) sol–gel, crystal violet (CV) photosensitizer, and hydrophobic electronegative molecules of 1H, 1H, 2H, 2H-perfluorooctyltriethoxysilane (PFOTES). The transparent Si-Al matrix strongly immobilized the photosensitizer molecules while dispersing them spatially, thus suppressing self-quenching. During nanolayer formation, PFOTES was anisotropically rearranged on the Si-Al matrix, promoting moisture resistance and triboelectric charging of the Si-Al/PFOTES-CV (SAPC)-coated filter. The SAPC nanolayer stabilized the photoexcited state of the photosensitizer and promoted redox reaction. Compared to pure-photosensitizer-coated filters, the SAPC filter showed substantially higher photobiocidal efficiency (~99.99 % for bacteria and a virus) and photo-durability (~83 % reduction in bactericidal efficiency for the pure-photosensitizer filter but ~0.34 % for the SAPC filter after 72 h of light irradiation). Moreover, after five washes with detergent, the SAPC filter maintained its photobiocidal and filtration performance, proving its reusability potential. Therefore, this SAPC nanolayer coating provides a practical strategy for manufacturing an antimicrobial and reusable mask filter for use during the ongoing COVID-19 pandemic.

1. Introduction

Controlling airborne microorganisms (called bioaerosols) is vital for protecting public health. In the 21st century, bioaerosols have threatened public health in various forms, from severe acute respiratory syndrome in 2002, to pandemic influenza A in 2009, to Middle East respiratory syndrome coronavirus in 2012 and COVID-19 in 2019 [1–4]. COVID-19 is still an ongoing threat, with more than 310 million

infections and 5.4 million deaths worldwide (as of 11 January 2022) [5]. Air filters are used in several devices, such as face masks, air purifiers, and ventilation systems, to suppress the spread of pathogens. In particular, face masks are the last redoubt protecting the respiratory tract, but their role is merely to block airborne pathogens physically. The bioaerosols captured on fibers can cause cross-contamination or diffuse out during disposal and recycling; [6] therefore, there is a need to develop innovative bioaerosol-inactivating materials. Various advanced fibers composed of organic or inorganic antimicrobial materials, such as copper, silver nanoparticles, chitosan, and natural products, have been developed to filter against bioaerosols [7–9]. However, these air filters effectively inactivate only microorganisms in direct contact with anti-microbial agents; therefore, their effectiveness gradually decreases as dust accumulates over the antimicrobial material. In addition, conventional filter disinfection technologies based on ultraviolet (UV) irradiation, plasma, and thermal energy have been developed; however, these technologies require additional energy and devices [10–12].

Recently, visible-light–driven (VLD) biocidal technologies, based on sunlight or indoor light energy, have been a focus of research in the field of photocatalysis [13,14]. VLD biocidal surfaces or air filters have been prepared using photosensitizing dyes such as triarylmethane, pheno-thiazine, and xanthene derivatives [15,16]. The dyes absorb visible photons and become photoexcited, triggering the generation of reactive oxygen species (ROS). The oxidative ROS can enable non-selective disinfection of pathogens by damaging the cell membrane, DNA, and RNA [17]. The photosensitizing dyes are inexpensive and have various applications; however, because of their high affinity to water, they easily leach into the environment when they come into contact with moisture [18]. To become incorporated into polymer fibers, the dyes need to be firmly immobilized to guarantee the durability and washability of the fibers. Several researchers have reported techniques for immobilizing dye, such as the physical trapping of dyes based on the polymer swelling effect [19,20] and surface modification–assisted dyeing for enhanced electrostatic adsorption [14,15]. However, such manufacturing processes are generally time consuming and may produce a large amount of unbound material as waste during washing. Thus, in the current pandemic, a novel approach to VLD biocidal functionalization is urgently required for bio-protection fields in pandemic era.

Commercial face masks are generally disposable because they lose their filtration properties during washing. This resulted in a shortage of face masks during the initial phase of the COVID-19 pandemic [21]. However, once the supply of face masks stabilized, discarding the generated mask-waste became an environmental problem. In addition, because of concerns over airborne transmission, the consumption of air filters has increased exponentially, leading to more waste [22]. Therefore, given these environmental and economic impacts, constructing a washable antimicrobial filter with regenerable filtration properties has become vital.

We introduce a novel fiber functionalization method that uses silica-alumina sol–gel (SAS) to endow face masks with a fibrous membrane for photocatalytic biocidal activity and reusability. The transparent SAS matrix immobilizes crystal violet (CV) photosensitizer dye and binds electronegative 1H, 1H, 2H, 2H-perfluorooctyltriethoxysilane (PFOTES) molecules to its surface. Moreover, the SAS matrix enhances the dispersity of the photosensitizers (suppressing self-quenching) and protects them from degradation by ROS, enhancing the photodurability. Compared to a CV alone, the SAS/PFOTES-CV (SAPC) nanolayer produced more ROS *via* enhanced redox reaction and showed excellent bactericidal/virucidal efficiency (~99.99 %) under visible light irradiation (3 h, 7.2 mW cm^{-2}). Moreover, PFOTES bonded to the SAS thin film increased water resistance and triboelectrification ability of the filter. The SAPC filter maintained its filtration and antimicrobial properties after cyclic washing tests, which demonstrates the excellent reusability. Our SAPC-based nanocoating technology is applicable to various textiles used in face masks and protective clothing, and can control the spread of COVID-19 and other airborne contagious diseases.

2. Materials and methods

2.1. Preparation of the silica-alumina sol–gel

The SAS was prepared from aluminum tri-sec butoxide (97 %; Sigma-Aldrich, USA), acetylacetone (99 %; Sigma-Aldrich), anhydrous 2-propanol (99.5 %; Sigma-Aldrich), methyltrimethoxysilane (95 %; Sigma-Aldrich), and 3-glycidylpropyltrimethoxysilane (GPTMS, 97 %; Sigma-Aldrich). First 20 g aluminum tri-sec butoxide, 5.4 g acetylacetone, and 5.4 g anhydrous 2-propanol were mixed and oil-bathed to form sol A. Then 30 g methyltrimethoxysilane, 17.3 g GPTMS, and 34 g anhydrous 2-propanol were mixed and oil-bathed to form sol B. Subsequently 21 g sol A was added to sol B, after which 37 g filtered water was added to form the SAS. The composite was refluxed at 80 °C for 12 h and then aged at room temperature for >24 h.

2.2. Preparation of the VLD antimicrobial filter

The SAS coating solution was prepared with a 10 wt% ethanol base concentration, and 1 wt% PFOTES (Sigma-Aldrich) was added to the solution to form SAS/PFOTES. Then 3 mM CV (Sigma-Aldrich) was mixed under steady agitation to form SAPC. Polypropylene melt-blown fabric with a basis weight of 32 g m^{-2} was procured from Filter Factory (CNS Industry, Suwon, Korea) (Table S1). All filter media were cleaned successively with acetone, ethanol, and isopropyl alcohol in an ultrasonic bath for 15 min each, and then oven-dried at 50 °C. The cleaned filters were treated with O$_2$ plasma for 3 min and dip-coated into the SAPC solution at a withdrawal rate of 0.5 mm s^{-1} (Fig. S1). The coated filters were cured at 50 °C for 2 h. The SAPC filters were rinsed with deionized water to remove residues and rounded to a 25.4 mm diameter to evaluate filtration and VLD antimicrobial performance.

2.3. VLD antimicrobial test

VLD antimicrobial performance was evaluated with two bacterial strains (*e.g.*, Gram-positive *Staphylococcus epidermidis* (*S. epidermidis*, Korean Collection for Type Cultures 1917) and Gram-negative *Escherichia coli* (*E. coli*, Korean Collection for Type Cultures 1039)) and MS2 bacteriophage (American Type Culture Collection 15597-B1). *S. epidermidis* and *E. coli* were incubated in a nutrient broth (beef extract 0.3 % and peptone 0.5 %; Becton Dickinson, USA) at 37 °C in a shaking incubator for 18 h. When the bacterial medium reached an optical density of ~0.6 at 600 nm, the bacteria were harvested *via* centrifugation (4,000×*g*, 15 min); washed in 10 mL phosphate-buffered saline (PBS) to remove undesirable broth; and then centrifuged to obtain the bacterial suspension, which then was resuspended in 10 mL PBS. The bacterial suspension was diluted to obtain ~10^8 CFU (colony forming unit) mL^{-1}. Host *E. coli* strain C3000 (American Type Culture Collection 15597) and MS2 bacteriophage were dispersed in tryptic soy broth (Difco Laboratories, Detroit, MI, USA) and incubated overnight at 37 °C in a shaking incubator. Then chloroform was added at a volume equal to the volume of the culture suspension and centrifuged (4,000×*g*, 20 min). The supernatant was extracted and transferred to 10 mL tryptic soy broth to prepare the bacteriophage solution. MS2 bacteriophage was assayed through the single agar layer method [23]. MS2 bacteriophage (0.1 mL) and log-phase host *E. coli* C3000 (0.3 mL) were mixed with 29.6 mL soft tryptic soy agar (Difco Laboratories). The tryptic soy agar mixture containing the bacteriophage was poured into 150 mm Petri dishes and then incubated at 37 °C until plaques became visible. The viral titer of the prepared bacteriophage solution was estimated to be ~10^{12} PFU mL^{-1}.

As shown in Fig. S2, 30 μL of the bacterial or bacteriophage solution was inoculated onto the control and SAPC filter surfaces, and then the samples were placed in a moisture box with a transparent glass cover. Sterilized wet cotton was also prepared to maintain constant humidity. The samples were then placed at a distance of 50 mm from an LED lamp

(CLA60 9.5 W; Osram; 400–800 nm wavelength) and illuminated at an intensity of 7.2 mW cm^{-2}, while an equal set of samples was kept in a dark box for the desired number of hours (Fig. S3). The resulting bacteria and bacteriophage samples were placed in 10 mL PBS and tryptic soy broth, respectively, and vortexed for 3 min to extract microbes from the samples into a suspension. The resulting bacterial suspension was serially diluted onto a nutrient agar plate (0.3 % beef extract and 0.5 % peptone; Becton Dickinson) and incubated at 37 °C for 24 h. The resulting bacteriophage suspension was serially diluted and plated using the single agar layer method. The antimicrobial efficiency was calculated using Eq. (1):

$$\text{Antimicrobial efficiency} = 1 - C/C_o \qquad (1)$$

where C and C_o are viable bacterial colonies or plaques from the SAPC and control filters, respectively.

2.4. VLD antimicrobial test against S. epidermidis aerosols

Fig. S4 shows the experimental configuration for supplying *S. epidermidis* bacterial aerosols to clean and dust-loaded SAPC filters. The prepared *S. epidermidis* solution was placed in a Collison nebulizer (BGI, Waltham, MA, USA) and aerosolized with clean air. During the aerosolization process, undesirable moisture was removed with a diffusion dryer, and bacterial particles were supplied to the test filter at a face velocity of 5.3 cm s^{-1}. The bacterial particle-deposited samples were placed in the aforementioned moisture box and exposed to visible light for 3 h while an equal set was placed in the dark box. The resulting samples were placed in 10 mL PBS containing 0.01 % Tween 80 and run through an extraction process (5 and 3 min of vortexing and sonication, respectively) to transfer the bacterial particles from the samples to PBS suspension. Finally, the suspension was serially diluted onto a nutrient agar plate and incubated at 37 °C for 24 h to determine CFU concentration.

2.5. Filtration test

MS2 bacteriophage aerosols were used to evaluate the filtration performance of uncharged and charged SAPC filters (Fig. S4). The prepared MS2 bacteriophage solution was purified *via* centrifugation at 6000×g for 20 min (Vivaspin 20; Sartorius Stedim Biotech) to remove undesirable nutrients and microbial by-products. Then 1 mL of the bacteriophage suspension was mixed with 9 mL of deionized water. The bacteriophage suspension was aerosolized by a Collison nebulizer and the bacteriophage particles were supplied to the test filters at a face velocity of 5.3 cm s^{-1}. The size distribution and number concentration of MS2 bacteriophage aerosols were measured with a scanning mobility particle sizer (model 3082; TSI, Shoreview, MN, USA). The filtration efficiency (η) was calculated using Eq. (2):

$$\eta = 1 - C_{outlet}/C_{inlet} \qquad (2)$$

where C_{inlet} and C_{outlet} represent the particle number concentration (particles cm$^{-3}_{air}$) of bacteriophage aerosols at the filter holder inlet and outlet, respectively.

2.6. ROS classification

The mechanism of VLD antimicrobial effects was evaluated with ROS scavengers or quenchers. Catalase, *L*-histidine, mannitol, and superoxide dismutase were purchased from Sigma-Aldrich. Catalase (2,000–5,000 units mg^{-1} protein) was used at a concentration of 6–14 units mL^{-1} in bacterial suspension to remove hydrogen peroxide. *l*-histidine was used as a singlet oxygen ($^1O_2$) quencher at a concentration of 2 mM in bacterial suspension. Mannitol was used at a concentration of 82 mM in bacterial suspension to eliminate hydroxyl radicals ($^\bullet$OH). Superoxide dismutase was used at a concentration of 20 units mL^{-1} in

bacterial suspension to remove superoxide radicals (O_2^-). *S. epidermidis* bacterial suspensions (~2.2 × 10^6 CFU mL^{-1}) containing a ROS scavenger or quencher were maintained in 3 mL glass bowls. SAPC filters were submerged in each bacterial suspension and irradiated with visible light at an optical power of 7.2 mW cm^{-2} for 4 h. The resulting bacterial suspension from each test was serially diluted onto a nutrient agar plate and incubated at 37 °C for 24 h. The bacterial colony concentration (CFU mL^{-1}) was determined for ROS classification.

2.7. Surface characterization

To analyze the surface of the VLD antimicrobial filter, we performed attenuated total reflection– Fourier-transform infrared (FTIR) spectroscopy (iS10; Thermo Fisher Scientific, USA) using a diamond crystal kit. Each specimen was analyzed over 32 scans with a resolution of 4 cm^{-1}, providing spectra in the range of 650–4,000 cm^{-1}. The surface of the VLD antimicrobial filter was characterized *via* X-ray photoelectron spectroscopy (XPS). Specimens were analyzed with an X-ray photoelectron spectrometer (NEXSA; Thermo Fisher Scientific) with Al K-alpha source (1,486.6 eV) in the range of 0–1,250 eV and at an angle of 90°. For in-depth profiling measurement, the surface was etched using an Ar ion source (0.5 KeV) at 20 and 60 s intervals for steps 1–14 and steps 15–29, respectively. The surface potential of the tested filter was measured with an electrostatic tester (FMX-004; Simco, Kobe, Japan) that could measure static voltages in the range of 0 to ±30 kV with an accuracy of ±10 %.

2.8. Photometric measurements

All UV–vis absorbance spectra were obtained with a UV–vis–NIR spectrometer (UV-3600Plus; Shimadzu, Japan). All absorbance measurements of the filter samples were conducted with specular component inclusion methods with an integrating sphere accessory (60 mm inner diameter, BaSO$_4$). Steady-state photoluminescence (PL) spectra at a wavelength of 600–800 nm were measured with a spectrophotometer (Fluorolog-3; Horiba Scientific, Japan) under 532 nm excitation. A time-resolved PL lifetime study was performed with an inverted-type scanning confocal microscope (SP8 FALCON; Leica Microsystems, Germany) with a 40× (air) objective lens. A picosecond laser line (594 nm, 40 MHz) from a white-light laser was used as an excitation source. A hybrid photon detector was used to collect emissions in the range of 600–750 nm from the samples. Fluorescence lifetime images of 512 × 512 pixels were simultaneously recorded with a galvo stage and time-correlated single-photon counting. Exponential fittings for the recorded fluorescence decays were applied using Leica software (LAS X v.3.5.5). Singlet oxygen ($^1O_2$) phosphorescence was measured with a near-infrared sensitive thermoelectrically cooled photomultiplier. The test filters were placed onto a glass slide and irradiated with a neodymium-doped yttrium aluminum garnet laser operating at 532 nm. $^1O_2$ phosphorescence was measured at a wavelength of ~1270 nm with a PC-mounted multi-scaler board with a pre-amplifier (MSA-300; Becker-Hickl, Germany) as the photon counter. Then the data were analyzed with FluoFit (PicoQuant, Germany).

2.9. Microscopic measurements

The morphologies of the samples were characterized *via* field-emission scanning electron microscopy (SEM) (MIRA3 LM; TESCAN, Czech Republic) under an accelerating voltage of 5.0 kV. Elemental distribution was obtained *via* energy-dispersive X-ray spectroscopy (EDS) coupled with field-emission SEM. Atomic-resolution EDS elemental maps of F and Al were collected. The image of the MS2 bacteriophage particles obtained using a transmission electron microscopy (Titan F20G; FEI, Hillsboro, OR, USA).

2.10. Water contact angle

The equilibrium water contact angles of the CV and SAPC filters were determined with a drop-shape analysis system (DSA100; KRUSS, Germany) in static mode with 4 μL deionized water droplet. The angle was measured at three locations on the test filter surface, and then the images were analyzed.

2.11. Leaching and washability test

For the leaching test, SAPC filters with various concentrations of SAS (wt%) were cut to 3 × 3 cm and vortexed in 15 mL of deionized water. The residue leached in deionized water was analyzed *via* UV–vis spectroscopy. A washability test was conducted according to American

Association of Textile Chemists and Colorists Test Method 61–2003. A commercial face mask and SAPC filters were immersed in 200 mL of deionized water with 0.37 % detergent. The mixture was stirred (40 rpm) for 45 min at 40 °C, and then the samples were rinsed with deionized water to remove residues. The samples were dried for 3 min at 60 °C, after which filtration and antimicrobial performance were evaluated for several cycles.

3. Results and discussion

3.1. Fabrication of the SAPC air filter

We consider the following factors in the development of our reusable VLD biocidal air filter: (i) leaching of photosensitizers, (ii)
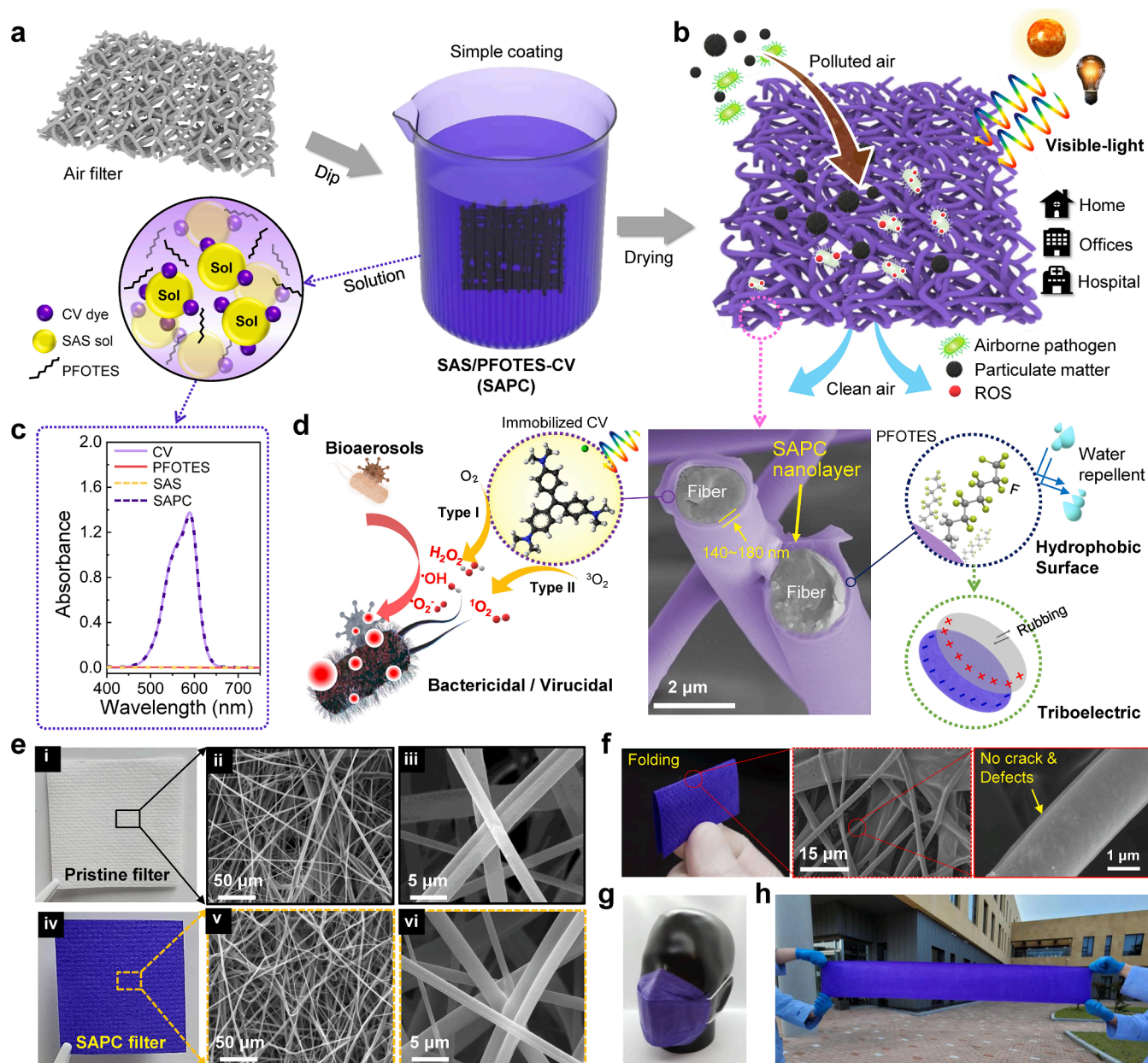

Fig. 1. Fabrication and function of the SAPC filter. (a) Schematic of the SAS-based nanocoating process. (b) Illustration of the broad applications of the SAPC filter with VLD biocidal activity. (c) UV–vis spectra of the CV, PFOTES, SAS, and SAPC solution. (d) Cross-sectional SEM image of the SAPC nanolayer on filter fibres (middle); descriptions of its photobiocidal (left) and hydrophobic/triboelectric (right) characteristics. (e) Photographs and SEM images of a pristine filter (i–iii) and the SAPC filter (iv–vi). (f) Folding test of the SAPC filter; photograph of the folded SAPC filter (left) and SEM images of the marked area (middle and right). (g) Prototype for the face mask application. (h) Demonstration of a large-scale 120-cm-long SAPC filter.

photodurability, (iii) regenerable filtration performance, and (iv) practical processibility. Our air filter incorporates a transparent and triboelectrically activated nanolayer in which photosensitizers are stably immobilized by electrophysical interactions.

The photobiocidal–triboelectric air filter was fabricated *via* a single-step nanocoating technique (Fig. 1a and S1). The coating solution consisted of SAS, PFOTES, and CV homogeneously dispersed in an ethanol base. The overall process consisted of dipping and curing. The methods are detailed in the Methods section. First, we synthesized a transparent SAS coating solution, which ensured the stable immobilization and uniform dispersion of CV dye during condensation polymerization. The SAS consisted of Al sol and GPTMS as a coupling agent. These constituents enhanced the mechanical and flexible properties of the SAS through the ring-opening of glycidyl silane and promoted the formation of linear siloxanes and polymerization [24,25]. Consequently, SAPC could form a nanolayer and fasten the CV onto the fiber surface within a short time and at low temperatures. The SAPC nanolayer could provide VLD biocidal activity over the fiber surface without compromising the filtration and air permeability functions of the fibrous membrane

(Fig. 1b). Thus, the SAPC filter can be utilized in homes, offices, and hospitals under indoor light conditions to improve the quality of the indoor air against airborne pathogens.

As shown in the UV–vis spectra (Fig. 1c), the maximum absorption wavelength (λ_{max}) of the SAPC solution appeared at 590 nm, consistent with the absorption wavelength of the CV, which indicates that the light absorption property of the CV was not influenced by the SAS or PFOTES. Fig. 1d shows a SEM image of the cross-section of the SAPC nanolayer covering the fiber and demonstrates its key functions (in purple). The CV immobilized inside the transparent SAS matrix produced ROS *via* a photochemical reaction, endowing the filter with bactericidal/virucidal properties. In addition, PFOTES enhanced the moisture resistance and provided high-electronegativity fluorinated surfaces favorable to triboelectric effects.

SEM results revealed that the SAPC nanolayer was stably produced on the surface and maintained its intrinsic physical structure without pore clogging (Fig. 1e). The EDS mapping results of the SAPC filter showed the presence of both aluminum (Al; blue-green dots) and fluorine (F; yellow dots) over the fiber surface (Fig. S5). Fig. 1f shows SEM
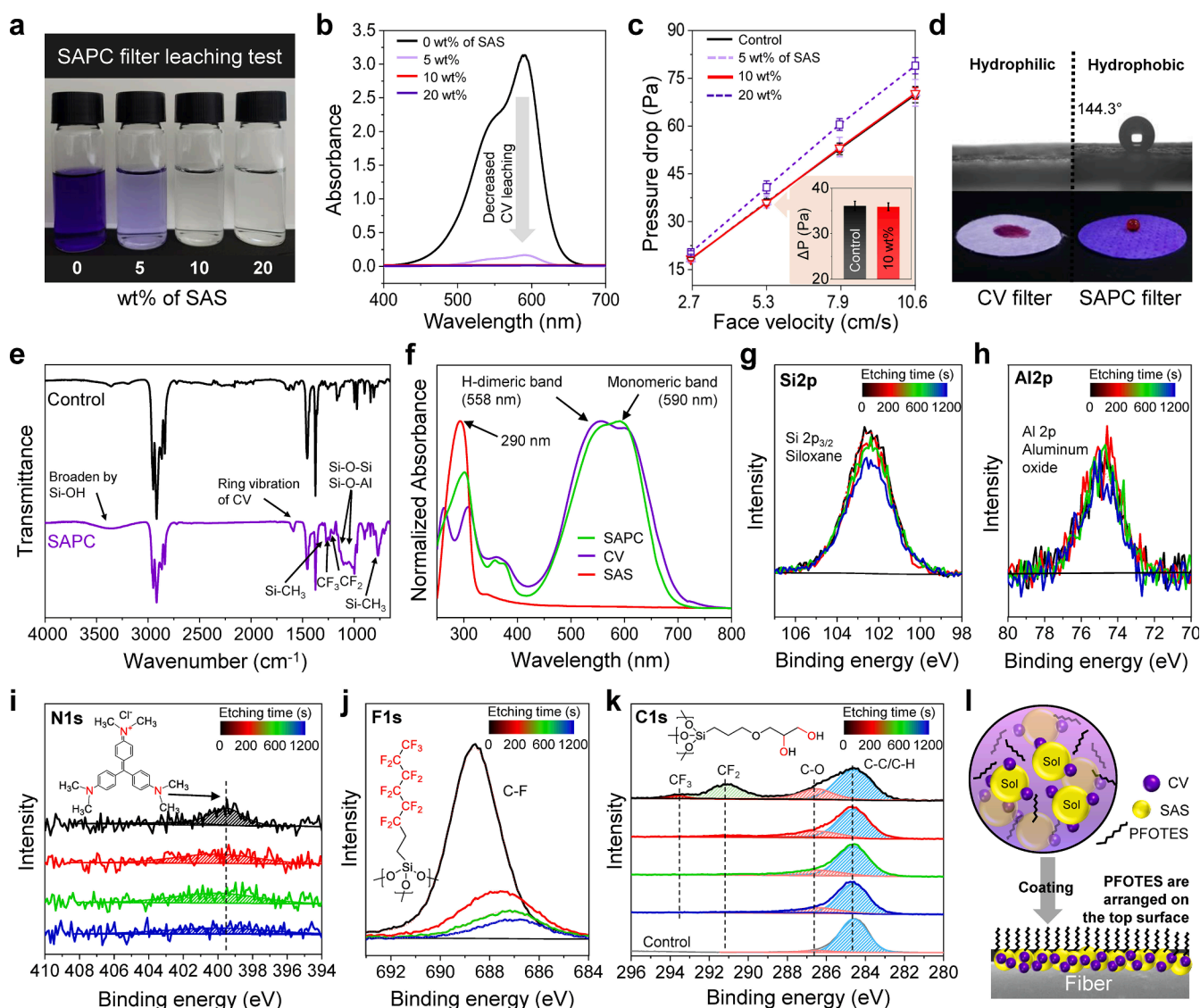

Fig. 2. Physical and structural characteristics of the SAPC filter. (a) Photos and (b) UV–vis spectra of the leaching solution by SAS concentration. (c) Pressure drop curves of filters prepared with different concentrations of SAS. (d) Static water contact angle measurements; sessile drop test results for the CV filter (top left) and SAPC filter (top right); red pigment was added for visuality. (e) FTIR spectra of the control and SAPC filters. (f) Diffuse-reflective UV–vis spectra of the SAPC, CV, and SAS filters. XPS depth profiling of the SAPC filter: (g) Si 2p, (h) Al 2p, (i) N 1 s, (j) F 1 s, and (k) C 1 s spectra. (l) Schematic of the SAPC layer structure. (For interpretation of the references to color in this figure legend, the reader is referred to the web version of this article.)

images of the folded SAPC filter. The folded fiber surfaces exhibited no cracks, which indicates good flexibility of the SAPC nanolayer, suitable for the manufacturing of pleated filters. These characteristics of the SAPC fibers are suitable for application as face masks and the demonstration using SAPC filter for face mask design is shown in Fig. 1g. Moreover, the proposed coating method is easy to scale up and applicable to various fabrics, such as polyester, cotton, and nylon (Fig. 1h and S6).

3.2. Physical stability and structural characteristics of the SAPC nanolayer

Given the importance of a waste-free, environmentally sustainable filter functionalization process, we conducted a leaching test to quantitatively determine the amount of unbound residue washed away from as-coated filters. Fig. 2a displays the first leaching solutions obtained from filters prepared with various concentrations of SAS (wt%). Concentrations of the CV and PFOTES were fixed at 3 mM and 1 wt%, respectively, and the SAS-free filter (hereafter "CV filter") was fabricated *via* the swell–encapsulation–shrink method [20]. As the concentration of SAS increased, the amount of leached dye decreased significantly. The UV–vis spectra of each leaching solution showed the outstanding dye immobilization ability of the SAPC matrix (Fig. 2b). Based on the λ_{max} of 590 nm, the amount of CV leached from the filter with 10 wt% SAS (0.008 ppm) was less than that from the CV filter (15 ppm). No residues were observed at higher concentrations of SAS, which demonstrates the eco-friendliness of our coating method. In addition, the air filter quality was affected by pressure drop. Because pressure drop is an important indicator of the energy efficiency of a filter, pore clogging should be avoided during the coating process. The pressure drop values of the filters with 5 and 10 wt% SAS were comparable to those of the pristine filter (*i.e.*, the control), whereas that of the filter with 20 wt% SAS was only 12.9 % higher (Fig. 2c). Therefore, the optimal SAS concentration for not damaging the air permeability of the filter was 10 wt%; an insignificant increase in pressure drop was also verified when the SAPC coating was applied to various commercial face mask layers (Fig. S7).

A drawback of using CV is its poor moisture stability [26]. However, the hydrophobic nature of PFOTES greatly improved the moisture resistance of the SAPC filter. The filter had a high water contact angle of 144.3°, whereas the CV filter was completely wet (Fig. 2d). The enhanced hydrophobicity mitigated the affinity of the dye to water, thereby inhibiting leaching (Fig. S8 and Movie S1). In addition, PFOTES containing perfluorinated compounds may be regarded as hazardous substances, and therefore should not be separated from the SAPC layer. Accordingly, we confirmed the binding stability of the SAPC by evaluating the leaching and fragmentation potential under harsh conditions (Table S2 and Fig. S9).

The main functional groups in the SAPC thin film were characterized *via* FTIR spectroscopy (Fig. 2e). Unlike the control spectrum, the SAPC filter spectrum showed major peaks of siloxane (1,000–1,100 cm^{-1}), Si-CH$_3$ (1,270 cm^{-1}), CF$_3$ (1,241 cm^{-1}), and CF$_2$ (1,197 cm^{-1}) [27,28]. A vibration band at 1,589 cm^{-1} and stretching band at 1,167 cm^{-1} confirmed the presence of aromatic rings and carbon rings of CV, respectively (Fig. S10) [29].

The light absorption properties of the SAS, CV, and SAPC filters were explored *via* diffuse-reflective UV–vis spectroscopy. The λ_{max} of the SAS filter appeared in the UV region (~300 nm), with negligible absorbance in the visible light region (400–800 nm; Fig. 2f). The optical transparency of the SAS matrix was favorable to the VLD photochemical reaction of the CV. The CV filter showed a high-intensity H-dimeric band at 558 nm because of the stacking of vertically oriented CV molecules and high-order aggregates [30]. Because the dimerization of CV inhibits electron or energy transfer by self-quenching photoexcited CV, it is unfavorable to ROS generation [16,30]. However, the SAPC filter showed a monomeric band at 590 nm, the same as that exhibited by the

solution form, which indicates dimerization inhibition [31]. It is attributable to the improved dispersity of the CV dye in the SAS matrix, caused by electrostatic interaction between cationic CV molecules and SAS matrix *via* hydrogen bonding [32].

The structural characteristics of the SAPC filter were investigated *via* etched XPS. The XPS surveys of the control and SAPC filters are shown in Fig. S11. The Si 2p and Al 2p spectra showed that the SAS matrix existed within an etching time of 1,180 s (Fig. 2g and h). N 1s spectra of CV dye were continuously detected during the etching time, which indicates that the CV was well spatially distributed in the SAS matrix (Fig. 2i). However, the F 1s spectra corresponding to PFOTES decreased with increasing etching time (Fig. 2j). The C–F bond of PFOTES was rearranged to the SAPC thin film surface during the crosslinking process to minimize surface energy. The C 1s spectra also showed that CF$_3$ and CF$_2$ bonds were dominant on the SAS layer (Fig. 2k) [33]. Meanwhile, the C–O bond of GPTMS, a major component of the SAS matrix, was homogeneously distributed inside the coating layer.

The structure of the SAPC nanolayer was derived according to these analyzes (Fig. 2l and S12). In the coating process, through a condensation reaction, the SAS bound with hydroxyl groups on the plasma-treated fiber surface and was crosslinked with the hydroxyl groups. The PFOTES molecules self-arranged on the SAS surface and bound with the SAS through a condensation reaction. Consequently, an integrated thin layer was formed. CV dye was evenly immobilized in the transparent SAS matrix, and PFOTES was prevalently attached to the matrix surface.

3.3. VLD biocidal activity of the SAPC filter

Fig. 3a depicts the time-dependent VLD bactericidal performance of the SAPC filter against *S. epidermidis*. All antimicrobial tests were conducted under a visible light intensity of 7.2 mW cm^{-2} unless otherwise stated. After 2 h of exposure to light, the photobiocidal activity of the SAPC filter increased rapidly, and bacteria were completely inactivated (~99.9999 %) after 4 h. It is important to note that the SAPC filter exhibited insignificant biocidal properties under dark conditions, which implies that the reduction in bacteria was due solely to a VLD photochemical reaction. Fig. 3b shows the bactericidal efficiency of filters prepared with various combinations of the SAPC layer constituents. After 3 h of illumination with visible light, the photobiocidal activities of the SAS- and SAS/PFOTES-coated filters were insignificant (0.24 and 0.22-log reduction, respectively). By contrast, the photobiocidal activity of the SAPC filter was higher (4.16-log reduction) than that of the CV filter (1.30-log reduction).

The Jablonski diagram in Fig. 3c illustrates the photochemical ROS generation mechanism of photosensitizers. Under light irradiation, photon-absorbed CV molecules transformed from a ground state (S$_0$) into a single excited state (S$_1$). The molecules at S$_1$ returned to S$_0$ through energy loss or transformed into a triplet excited state (T$_1$) *via* intersystem crossing. The CV molecules in the triplet state underwent a Type-I and/or Type-II photochemical reaction. In the Type-I pathway, they underwent redox reactions, leading to the generation of superoxide anion (O$_2^-$), hydrogen peroxide (H$_2$O$_2$), and hydroxyl radical (•OH). In the Type-II pathway, energy at T$_1$ was transferred to triplet oxygen (^{3}O$_2$) *via* Dexter energy transfer, resulting in the generation of singlet oxygen (^{1}O$_2$) [34,35]. To study the photoreaction mechanism of the enhanced biocidal activity, we measured time-resolved PL decays for the CV and SAPC filters (Fig. 3d). The PL average lifetime of the CV layer (0.991 ns) was approximately 5.4 times longer than that of the SAPC layer (0.182 ns; see Table S3). The significant difference in PL lifetime is reflected in the fluorescence lifetime imaging microscopy results. The SAPC filter had a shorter lifetime distribution on the overall fiber area. In addition, the SAPC filter exhibited a lower PL peak intensity than the CV filter (Fig. S13), which indicates that it had a lower radiative deactivation rate of photoexcited electrons than the CV filter. These results reveal that the SAS matrix can enhance the excited state of CV sensitizers to provide
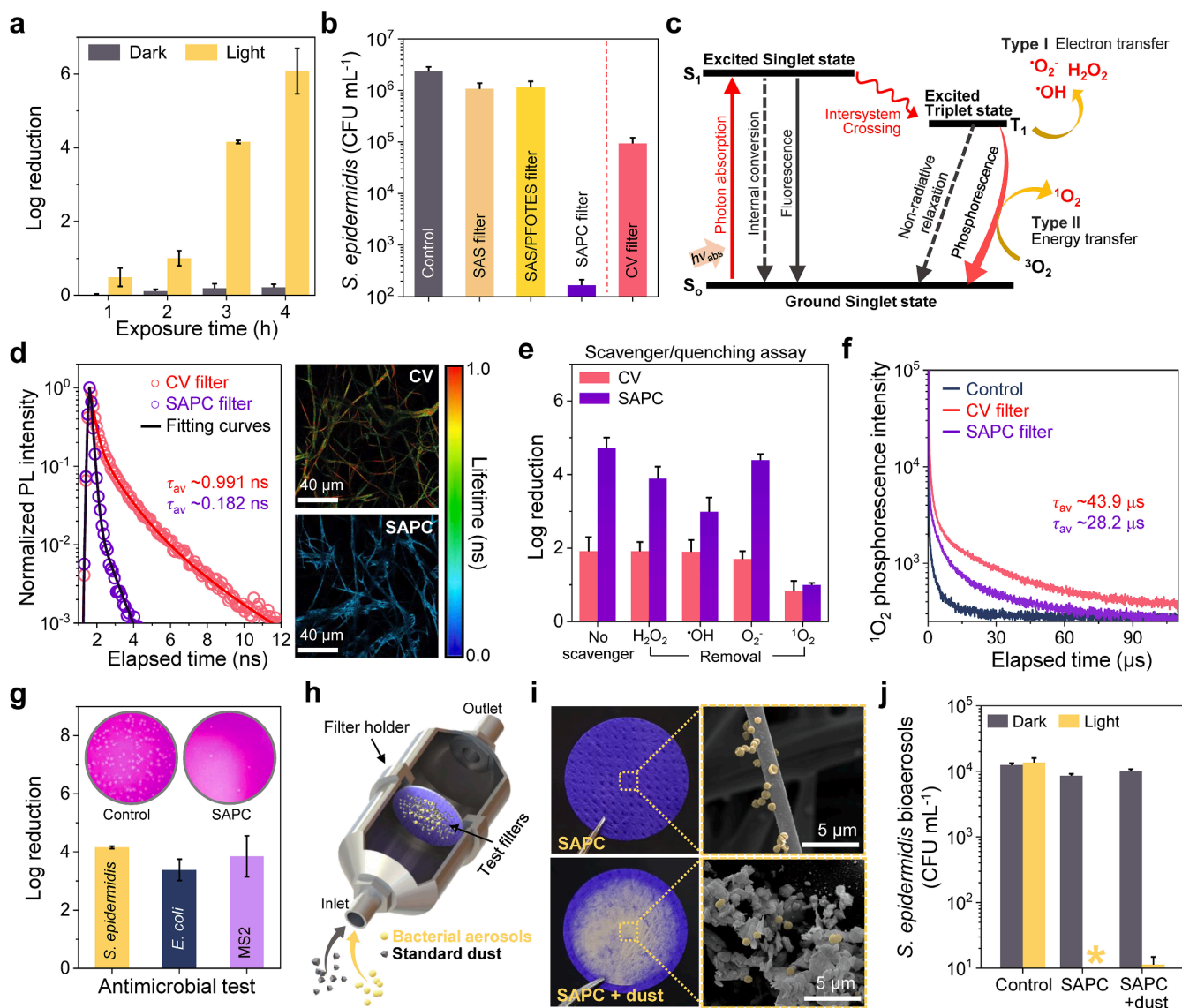
Fig. 3. Photobiocidal performance and underlying mechanisms of the SAPC filter. (a) Photobiocidal activity against *S. epidermidis* by duration of light exposure. (b) Antimicrobial activity of filters prepared with various combinations of the SAPC nanolayer constituents. (c) Jablonski diagram describing photochemical processes. (d) Time-resolved photoluminescence decay of the CV and SAPC filters (λ_{Ex} = 594 nm, λ_{Em} = 600–750 nm) and results of fluorescence lifetime imaging microscopy. (e) Bacterial inactivation according to scavenger/quenching assay. (f) Time-resolved $^1O_2$ phosphorescence decay for the CV and SAPC filters. (g) Photobiocidal activity against *S. epidermidis*, *E. coli*, and MS2 bacteriophage. The insets present the visible plaque of MS2 bacteriophage. (h) Bioaerosol test device. (i) Photographs and SEM images of bare (top) and dust-loaded (bottom) SAPC filters on which bacterial particles were deposited. Bacterial particles are colored yellow. (j) Bactericidal performance of the bare and dust-loaded SAPC filters against bacterial bioaerosols; the asterisk represents the region below the detection limit: <10 CFU mL^{-1}. (For interpretation of the references to color in this figure legend, the reader is referred to the web version of this article.)

more efficient ROS generation *via* redox or energy transfer pathways [16,36,37].

ROS scavenger/quenching analyzes were conducted using *S. epidermidis* to determine the ROS species that contributed to bactericidal activity in the SAPC filter (Fig. 3e). To prevent miscalculation related to dye leaching from the CV filter, the CV was immobilized in polydimethylsiloxane (PDMS) *via* the swell–encapsulation–shrink method. When H$_2$O$_2$, $^•$OH, and O$_2^-$ were scavenged with the addition of catalase, mannitol, and superoxide dismutase, respectively, the CV-PDMS filter exhibited insignificant change in bactericidal activity compared to the SAPC filter. In particular, after $^•$OH scavenging, the bactericidal activity of the SAPC filters was reduced by ~37 % compared to no scavenger, which suggests that the SAPC nanolayer promoted a redox reaction. After the addition of L-histidine (a $^1O_2$ quencher), the bactericidal activity of both the CV-PDMS and SAPC filters decreased to ~0.8 and ~1-log reduction, respectively. The SAPC layer showed considerably higher

$^•$OH generation than CV-PDMS, but it was not clear whether the SAPC enhanced the Type-I photoreaction. Thus, we measured the $^1O_2$ phosphorescence lifetime *via* time-resolved near-infrared spectroscopy. Fig. 3f shows the $^1O_2$ phosphorescence decay of the SAPC, CV, and control filters at a wavelength of 1,270 nm. The $^1O_2$ lifetime of the CV filter (~43.9 μs) was approximately 1.5 times longer than that of the SAPC filter (~28.2 μs). The shorter $^1O_2$ lifetime of the SAPC filter indicates the competitively attenuated the Type-II photoreaction.

Fig. 3g demonstrates the non-selective inactivation performance of the SAPC filter against various microbes (visible light exposure for 3 h). MS2 bacteriophage was selected as a surrogate virus because it is similar to pathogenic viruses in size and morphology and has been utilized in various survival studies [38]. The VLD photobiocidal activity of the SAPC filter was lethal to gram-negative bacteria (*E. coli*) and MS2 bacteriophage (>99.9 % biocidal efficiency). We further examined antimicrobial performance under stronger sunlight conditions

(Fig. S14). Under sunlight conditions, photobiocidal activity reached ~96.8 % after 30 min and was completely inactivated in 1 h. These results indicate the practicability of the SAPC filter for use in indoor and outdoor environments without additional devices.

In a real air environment, the ratio of airborne microorganisms to total particulate matter is generally low. However, high concentrations of pathogenic bioaerosols are generated by specific events such as the physical activity of an infected individual [39]. Thus, bioaerosols can be captured in both filter fibers and pre-accumulated particulate matter. To determine the photobiocidal activity of the SAPC filter in a dust-rich environment in which most photo-active sites were shielded, we conducted antimicrobial tests using aerosolized bacterial particles. Fig. 3h shows an image of the bioaerosol testing device. The bacterial aerosols exhibited a log-normal size distribution, with a peak diameter of 0.9 μm and a number concentration of ~880 particles cm^{-3}_{air} (Fig. S15). Bacterial aerosols were deposited onto clean and dust-loaded SAPC filters. The dust-loaded SAPC filter was prepared according to a dust holding capacity (DHC) of 4.3 g m^{-2}, equal to 2.5 times the initial pressure drop (Table S4) [40]. SEM images showed that bacterial particles were captured on the dust rather than the SAPC filter surface (Fig. 3i). It is interesting that the SAPC filter retained its robust antimicrobial activity even under the dust-accumulation condition, leading to a consistent ~3-log reduction in *S. epidermidis* (Fig. 3j). These results are related to the ability of generated $^1O_2$ to diffuse 0.992 cm into the air [41]. This photobiocidal activity has the potential to solve the problem of the deterioration in antimicrobial performance caused by the accumulation of dust in conventional antimicrobial air filters that operate based on the direct contact killing mechanism.

3.4. Photodurability enhancement by the SAPC nanolayer

Owing to photooxidation, the photobiocidal activity of the dye progressively dissipated during long-term use under light irradiation.

Fig. 4a shows different photofading behaviors of the CV and SAPC filters under visible light irradiation (7.2 mW cm^{-2}). The CV filter was rapidly decolorized after 24 h of exposure to light. By contrast, the SAPC filter hardly changed color even after 120 h, which demonstrates its low photodegradability.

Furthermore, the photodecomposition of each filter sample was examined using diffuse-reflective UV–vis absorption spectroscopy. The inhibition process of CV photodegradation was suggested to involve two mechanisms: demethylation via •OH attack of the N-dimethyl position, and ketone formation through •OH and $^1O_2$ attacks of the central phenyl-substituted carbon (Figs. S16 and S17) [42]. The partially electronegative oxygen atom of the SAS matrix exhibits strong electrostatic interactions and hydrogen bonding with the nitrogen atom of CV dye molecules, resulting in their encapsulation [43,44]. The SAS encapsulation can significantly prevent demethylation of CV molecules by protecting against ROS attack and dye leaching from the coating layer. The light-exposed CV filter showed rapid photooxidation and a distinct hypsochromic shift of the monomeric band from 600 to 580 nm (Fig. 4b), characteristic of the formation of demethylated derivatives of the CV by ROS attack [45]. The peak shift from 1,587 to 1,596 cm^{-1} in the infrared spectra of the CV filter also indicated CV demethylation (Fig. S18) [46]. Moreover, the SAPC filter showed substantially less reduction in absorbance (~5.3 %; regarding the integrated area over the visible region) than the CV filter (~47.2 %) under exposure to 96 h of light (Fig. 4c). These results show that the SAS matrix suppressed CV degradation by protecting the dye from ROS attacks.

Fig. 4d describes the possible mechanism of photodurability enhancement by SAS encapsulation. The two putative mechanisms are as follows: First, hydrogen bonding of the SAS matrix, which protected the nitrogen atoms of CV molecules from highly electrophilic ROS attacks, inhibited demethylation. Second, electron-rich oxygen atoms around the CV in the SAS matrix attracted ROS; thus, it was difficult for the ROS to reach the central phenyl-substituted carbon, inhibiting
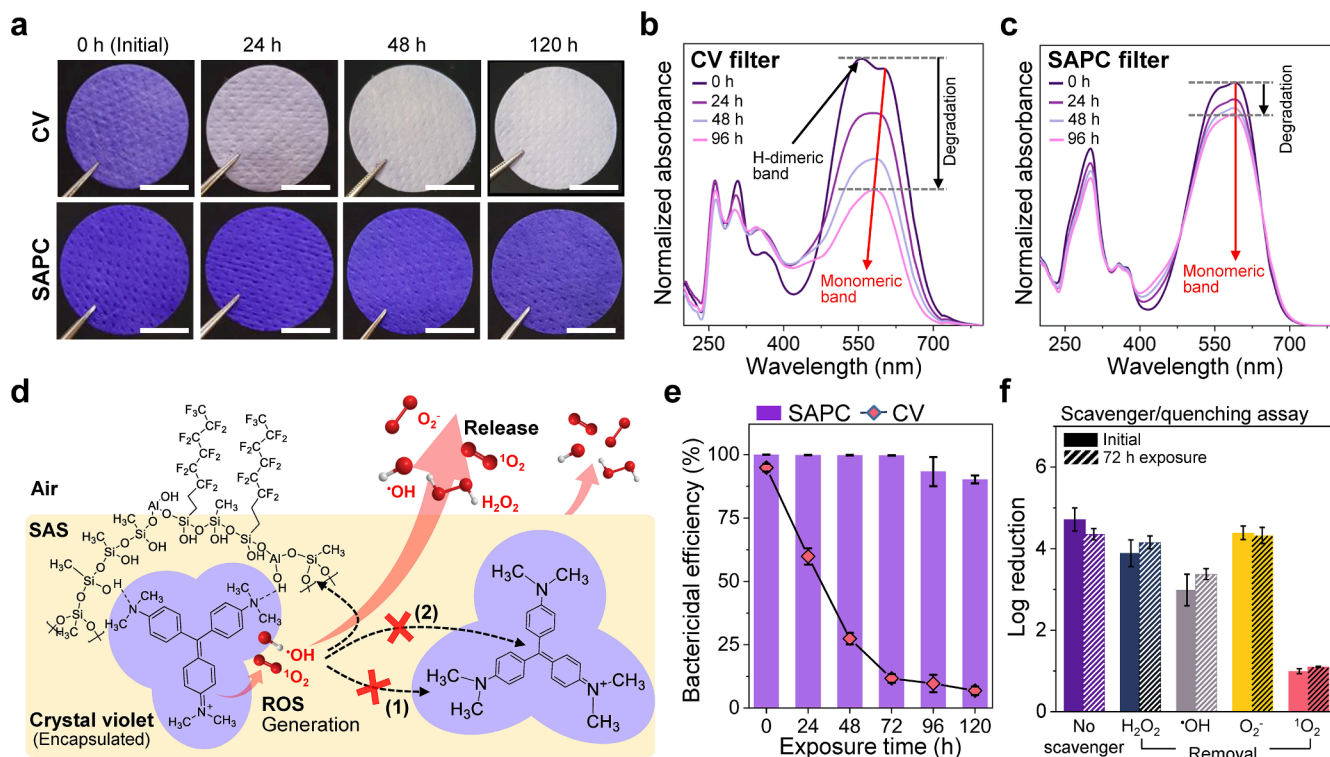

Fig. 4. Photodurability of the SAPC filter. (a) Photos of photooxidation tests of the CV and SAPC filters; scale bars indicate 10 mm. (b, c) Diffuse-reflective UV–vis absorbance spectra of the CV and SAPC filters under exposure to 96 h of continuous light. (d) Schematic of the photodurability enhancement mechanism; Preventing (1) demethylation and (2) ketone formation by ROS attacks. (e) Bactericidal efficiency of the CV and SAPC filters by duration of light exposure. (f) Comparison of the bacterial inactivation ratio according to scavenger/quenching assay of the initial and 72-h-light-exposed SAPC filters.

ketone formation. Consequently, the SAS matrix attenuated photooxidation of CV under ROS attack, and a higher SAS concentration resulted in better photodurability (Fig. S19).

Fig. 4e demonstrates the long-term bactericidal performance of the SAPC filter. The bactericidal efficiency of the CV filter decreased rapidly from 94.8 % to 59.9 % after 24 h and then to 6.85 % after 120 h. By contrast, the SAPC filter showed robust durability; its bactericidal efficiency hardly changed with up to 72 h of light exposure, which is equivalent to 9 days based on 8 business hours per day. After 120 h, the bactericidal efficiency was reduced by only 9.81 %. We investigated the ROS contributing to the bactericidal activity of the light-exposed SAPC filter using a scavenger/quenching assay (Fig. 4f). The bacterial inactivation of the SAPC filter exposed to light for 72 h decreased by only 0.36-log reduction compared to the initial value. But $^{\bullet}OH$ and $^1O_2$ were still the principal ROS for bactericidal activity. In summary, the SAPC nanolayer can provide prolonged photobiocidal activity by protecting the photosensitizers from ROS attack.

3.5. Triboelectric filtration performance

Triboelectric effects can restore electrostatic charges in filters with little energy and at low cost and can electrostatically enhance filtration efficiency without increasing pressure drop [47]. The surface of SAPC nanolayer contained a large number of PFOTES, mainly composed of fluorine (Fig. 2l). Fluorine is the highest electronegative element according to the Pauling scale, and fluorinated polymers such as polytetrafluoroethylene and polyvinylidene fluoride have been used as negative triboelectric materials [48,49]. We selected a nylon mesh, which is at the lower end of the positive triboelectric series, as a counter material to demonstrate the triboelectric effects of the SAPC filter (Fig. 5a). When the SAPC and nylon fibers were rubbed together, they became negatively and positively charged, respectively, and generated an electric field sufficient for the electrostatic capture of incoming particles (Fig. 5b). Fig. 5c shows the surface potential (V_s) of the SAPC, SAS/CV, and control filters according to the number of rubbing cycles. After five rubbing cycles, the V_s plateaued, indicating triboelectric charge saturation. The V_s of the SAPC filter (–5 kV) was 3.9 and 1.7 times that of the SAS/CV and control filters, respectively. The higher V_s of the SAPC filter was due to the superior electron acquisition ability of the PFOTES molecules bonded to the SAS layer. To evaluate the filtration performance of the triboelectrically charged SAPC filter, we utilized MS2 bacteriophage aerosols at a face velocity of 5.3 cm s^{-1} (Fig. 5d). The number concentration of MS2 aerosols decreased rapidly as they passed through the triboelectrically charged SAPC filters. The filtration efficiency of the charged SAPC filter was 95.5 %, approximately 20% higher than that of the uncharged SAPC filter.

The most common method for applying electrostatic forces to air filters is through corona discharge, which is also applicable to the SAPC filter (Fig. S19). However, the corona discharge method is not accessible in the home and may not be suitable for an electrostatic charge restoration process. The triboelectric effect is an efficient potential alternative for recovering electrostatic forces. We investigated the change in the V_s of the SAPC filter for several detergent washing cycles (Fig. 5e). After four washing cycles, the V_s was still more than –4.5 kV, having decreased by only ~9 %; thus, the recharged SAPC filter retained a filtration efficiency of >91 % after four washing cycles, while the efficiency of the commercial face mask decreased to 85 ± 1.1 %. (Fig. 5f). Although the SAPC filter was subjected to forceful dust loading and removal, its physical structure was intact, with no leaching problems. Furthermore, we evaluated the durability and reusability of the SAPC filter in terms of VLD antimicrobial activity. The filter was subjected to four washing runs, and its antimicrobial efficiency against *S. epidermidis* was tested after each run (Fig. 5g). The SAPC nanolayer maintained a high photobiocidal efficiency of >99.9 % after each washing run. These results
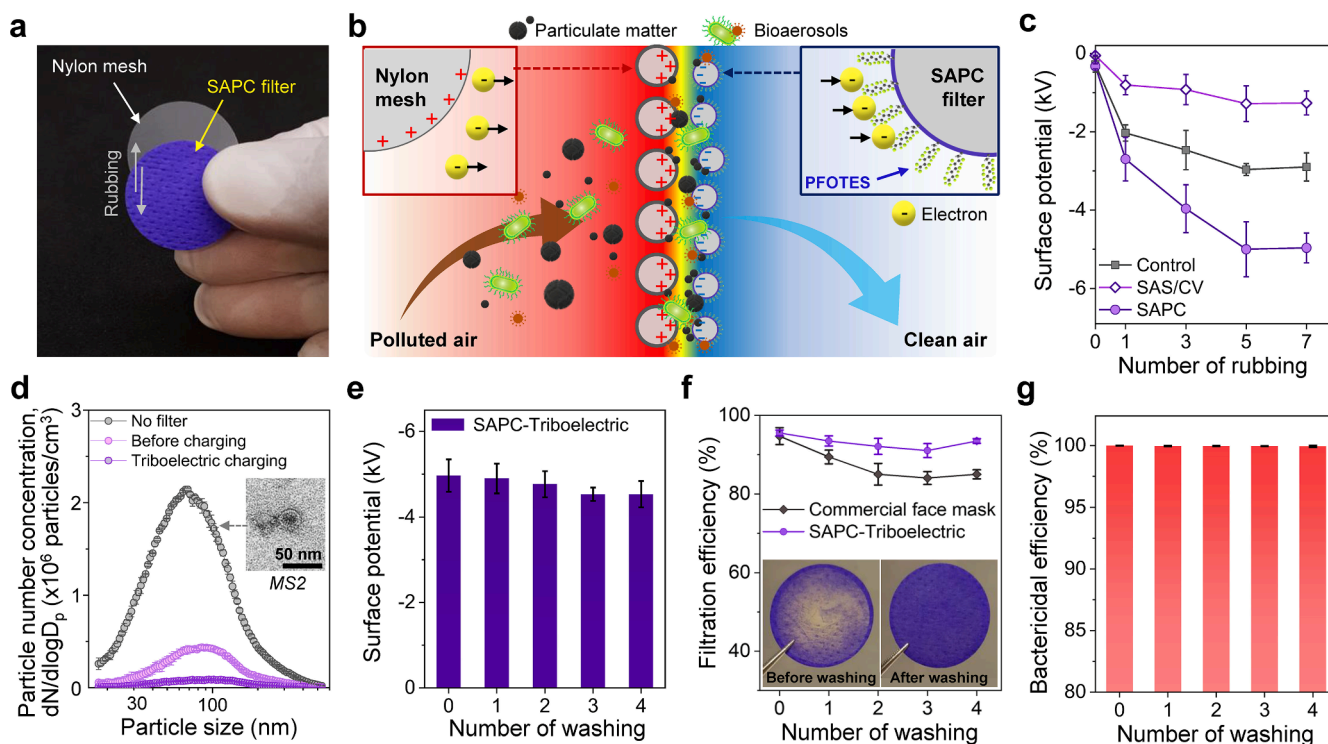

Fig. 5. Triboelectric filtration performance of the SAPC filter. (a) Rubbing process for examining triboelectric effects. (b) Schematic of the filtration mechanism of the charged SAPC filter. (c) Surface potential of the filters according to the number of rubbing cycles. (d) Particle size distribution of MS2 bacteriophage bioaerosols filtered by triboelectrically charged and uncharged SAPC filters. The inset presents a transmission electron microscopy image of the MS2 bacteriophage particle. (e) Change in the surface potential of the charged SAPC filter detergent-washed zero to four times. (f) Change in the filtration efficiency of the SAPC filter and a commercial face mask during a cyclic washing test. The insets present the unwashed and washed SAPC filters. (g) VLD antimicrobial efficiency of the SAPC filter against *S. epidermidis* during cyclic washing tests.

demonstrate the durability and reusability of the SAPC filter in terms of antimicrobial and filtration performance.

Based on photobiocidal performance, photodurability, and triboelectric activity data, we designed prototype face masks (Fig. S21). The SAPC coating can be applied to the outer or filtration layer of the face mask for effective protection against airborne pathogens. For the former, the photobiocidal properties of the SAPC coating can be partially transferred to the filtration layer. For the latter, when the outer layer is a transparent nylon mesh, photobiocidal activity and triboelectric effects can be exploited more efficiently. We are planning to further study to validate effectiveness of our designed masks.

4. Conclusion

We present a new approach to fabricating reusable, photobiocidal, triboelectric air filters using the SAPC-based nanolayer coating. The composite nanolayer comprised a transparent SAS matrix, matrix-embedded CV photosensitizer, and surface PFOTES, which endowed the filter with reusability and photobiocidal and triboelectric functionality. The SAPC nanolayer showed an enhanced redox reaction, resulting in high photobiocidal performance. Under indoor light conditions, the SAPC filter showed a high photobiocidal efficiency of ~4-log reduction against bacteria (*i.e.*, *S. epidermidis* and *E. coli*) and a surrogate virus (*i.e.*, MS2 bacteriophage). In addition, the SAS matrix attenuated photooxidation of CV under ROS attack, which improved longevity. Furthermore, during detergent washing tests, the SAPC filter retained its filtration performance and photobiocidal activity owing to its superior water stability and triboelectric characteristics, which demonstrates its good washability and reusability. Overall, the coating of SAPC nanolayer endowed the filter with enhanced photobiocidal activity, photodurability, and triboelectric property. Thus, the proposed method can be used to design of more efficient photobiocidal materials to protect the environment from infectious pathogens.

Declaration of Competing Interest

The authors declare that they have no known competing financial interests or personal relationships that could have appeared to influence the work reported in this paper.

Appendix A. Supplementary data

Supplementary data to this article can be found online at https://doi.org/10.1016/j.cej.2022.135830.

References

[1] Y. Li, X. Huang, I.T.S. Yu, T.W. Wong, H. Qian, Role of air distribution in SARS transmission during the largest nosocomial outbreak in Hong Kong, Indoor Air 15 (2) (2005) 83–95, https://doi.org/10.1111/j.1600-0668.2004.00317.x.

[2] A.M. Siston, Pandemic 2009 influenza A (H1N1) virus illness among pregnant women in the United States, JAMA 303 (15) (2010) 1517, https://doi.org/10.1001/jama.2010.479.

[3] A. Zumla, D.S. Hui, Infection control and MERS-CoV in health-care workers, The Lancet 383 (2014) 1869–1871, https://doi.org/10.1016/S0140-6736(14)60852-7.

[4] A. Nalbandian, K. Sehgal, A. Gupta, M.V. Madhavan, C. McGroder, J.S. Stevens, J. R. Cook, A.S. Nordvig, D. Shalev, T.S. Sehrawat, N. Ahluwalia, B. Bikdeli, D. Dietz, C. Der-Nigoghossian, N. Liyanage-Don, G.F. Rosner, E.J. Bernstein, S. Mohan, A. A. Beckley, D.S. Seres, T.K. Choueiri, N. Uriel, J.C. Ausiello, D. Accili, D. E. Freedberg, M. Baldwin, A. Schwartz, D. Brodie, C.K. Garcia, M.S.V. Elkind, J. M. Connors, J.P. Bilezikian, D.W. Landry, E.Y. Wan, Post-acute COVID-19 syndrome, Nat. Med. 27 (2021) 601–615, https://doi.org/10.1038/s41591-021-01283-z.

[5] "COVID-19 Dashboard." The Center for Systems and Engineering (CSSE) at Johns Hopkins University. https://coronavirus.jhu.edu/map.html.

[6] S.B. Jeong, H.S. Ko, S.C. Seo, J.H. Jung, Evaluation of filtration characteristics and microbial recovery rates of commercial filtering facepiece respirators against airborne bacterial particles, Sci. Total Environ. 682 (2019) 729–736, https://doi.org/10.1016/j.scitotenv.2019.05.153.

[7] S. Kumar, M. Karmacharya, S.R. Joshi, O. Gulenko, J. Park, G.H. Kim, Y.K. Cho, Photoactive antiviral face mask with self-sterilization and reusability, Nano Lett. 21 (2021) 337–343, https://doi.org/10.1021/acs.nanolett.0c03725.

[8] Y.-C. Chen, C.-H. Liao, W.-T. Shen, C. Su, Y.-C. Wu, M.-H. Tsai, S.-S. Hsiao, K.-P. Yu, C.-H. Tseng, Effective disinfection of airborne microbial contamination in hospital wards using a zero-valent nano-silver/TiO 2 -chitosan composite, Indoor Air 29 (3) (2019) 439–449, https://doi.org/10.1111/ina.12543.

[9] G.B. Hwang, K.J. Heo, J.H. Yun, J.E. Lee, H.J. Lee, C.W. Nho, G.-N. Bae, J.H. Jung, M. Yao, Antimicrobial air filters using natural Euscaphis japonica nanoparticles, PLoS ONE 10 (5) (2015) e0126481, https://doi.org/10.1371/journal.pone.0126481.

[10] L. Liao, W. Xiao, M. Zhao, X. Yu, H. Wang, Q. Wang, S. Chu, Y. Cui, Can N95 respirators be reused after disinfection? How many times? ACS Nano 14 (2020) 6348–6356, https://doi.org/10.1021/acsnano.0c03597.

[11] R.K. Campos, J. Jin, G.H. Rafael, M. Zhao, L. Liao, G. Simmons, S. Chu, S. C. Weaver, W. Chiu, Y.i. Cui, Decontamination of SARS-CoV-2 and other RNA viruses from N95 level meltblown polypropylene fabric using heat under different humidities, ACS Nano 14 (10) (2020) 14017–14025, https://doi.org/10.1021/acsnano.0c06565.

[12] F. Prehn, E. Timmermann, M. Kettlitz, K. Schaufler, S. Günther, V. Hahn, Inactivation of airborne bacteria by plasma treatment and ionic wind for indoor air cleaning, Plasma Process. Polym. 17 (2020) 1–12, https://doi.org/10.1002/ppap.202000027.

[13] P. Li, J. Li, X. Feng, J. Li, Y. Hao, J. Zhang, H. Wang, A. Yin, J. Zhou, X. Ma, B. Wang, Metal-organic frameworks with photocatalytic bactericidal activity for integrated air cleaning, Nat. Commun. 10 (2019) 2177, https://doi.org/10.1038/s41467-019-10218-9.

[14] Y. Si, Z. Zhang, W. Wu, Q. Fu, K. Huang, N. Nitin, B. Ding, G. Sun, Daylight-driven rechargeable antibacterial and antiviral nanofibrous membranes for bioprotective applications, Sci. Adv. 4 (2018) eaar5931, https://doi.org/10.1126/sciadv.aar5931.

[15] P. Tang, Z. Zhang, A.Y. El-Moghazy, N. Wisuthiphaet, N. Nitin, G. Sun, Daylight-induced antibacterial and antiviral cotton cloth for offensive personal protection, ACS Appl. Mater. Interfaces 12 (2020) 49442–49451, https://doi.org/10.1021/acsami.0c15540.

[16] S. Noimark, E. Salvadori, R. Gómez-Bombarelli, A.J. MacRobert, I.P. Parkin, C.W. M. Kay, Comparative study of singlet oxygen production by photosensitiser dyes encapsulated in silicone: Towards rational design of anti-microbial surfaces, Phys. Chem. Chem. Phys. 18 (2016) 28101–28109, https://doi.org/10.1039/C6CP02529C.

[17] F. Vatansever, W.C.M.A. de Melo, P. Avci, D. Vecchio, M. Sadasivam, A. Gupta, R. Chandran, M. Karimi, N.A. Parizotto, R. Yin, G.P. Tegos, M.R. Hamblin, Antimicrobial strategies centered around reactive oxygen species – bactericidal antibiotics, photodynamic therapy, and beyond, FEMS Microbiol. Rev. 37 (2013) 955–989, https://doi.org/10.1111/1574-6976.12026.

[18] K.J. Heo, S. Bin Jeong, J. Shin, G.B. Hwang, H.S. Ko, Y. Kim, D.Y. Choi, J.H. Jung, Water-repellent TiO₂-organic dye-based air filters for efficient visible-light-activated photochemical inactivation against bioaerosols, Nano Lett. 21 (2021) 1576–1583, https://doi.org/10.1021/acs.nanolett.0c03173.

[19] G.B. Hwang, H. Huang, G. Wu, J. Shin, A. Kafizas, K. Karu, H. Du Toit, A. M. Alotaibi, L. Mohammad-Hadi, E. Allan, A.J. MacRobert, A. Gavriilidis, I. P. Parkin, Photobactericidal activity activated by thiolated gold nanoclusters at low flux levels of white light, Nat. Commun. 11 (2020) 1207, https://doi.org/10.1038/s41467-020-15004-6.

[20] E. Ozkan, E. Allan, I.P. Parkin, The antibacterial properties of light-activated polydimethylsiloxane containing crystal violet, RSC Adv. 4 (2014) 51711–51715, https://doi.org/10.1039/C4RA08503E.

[21] M.L. Ranney, V. Griffeth, A.K. Jha, Critical supply shortages — the need for ventilators and personal protective equipment during the Covid-19 pandemic, e41, N. Engl. J. Med. 382 (18) (2020), https://doi.org/10.1056/NEJMp200614.

[22] S. Morgana, B. Casentini, S. Amalfitano, Uncovering the release of micro/nanoplastics from disposable face masks at times of COVID-19, J. Hazard. Mater. 419 (2021) 126507, https://doi.org/10.1016/j.jhazmat.2021.126507.

[23] U.S. Environmental Protection Agency, (EPA), "Method 1601: Male-specific (F+) and Somatic Coliphage in Water by Two-Step Enrichment Procedure" (Publication 821-R-01-030, EPA, 2001; www.epa.gov/sites/default/files/2015-12/documents/method_1601_2001.pdf). [the easiest access to this source is via the URL].

[24] Z. Zhang, Catalytic Effect of Aluminum Acetylacetonate on Hydrolysis and Polymerization of Methyltrimethoxysilane, Langmuir 13 (1997) 473–476, https://doi.org/10.1021/la960771+.

[25] T.H. Lee, E.S. Kang, B.S. Bae, Catalytic effects of aluminum butoxyethoxide in sol-gel hybrid hard coatings, J. Sol-Gel Sci. Technol. 27 (2003) 23–29, https://doi.org/10.1023/A:1022671625334.

[26] F. Bella, C. Gerbaldi, C. Barolo, M. Grätzel, Aqueous dye-sensitized solar cells, Chem. Soc. Rev. 44 (11) (2015) 3431–3473, https://doi.org/10.1039/C4CS00456F.

[27] W. Shen, L. Zhang, X. Li, H.Z. Yu, Binary silanization and silver nanoparticle encapsulation to create superhydrophobic cotton fabrics with antimicrobial capability, Sci. Rep. 9 (2019) 9172, https://doi.org/10.1038/s41598-019-45622-0.

[28] D.P. Dowling, C.E. Nwankire, M. Riihimäki, R. Keiski, U. Nylén, Evaluation of the anti-fouling properties of nm thick atmospheric plasma deposited coatings, Surf. Coat. Technol. 205 (2010) 1544–1551, https://doi.org/10.1016/J.SURFCOAT.2010.10.010.

[29] V. Sabna, S.G. Thampi, S. Chandrakaran, Adsorption of crystal violet onto functionalised multi-walled carbon nanotubes: equilibrium and kinetic studies, Ecotox. Environ. Safe. 134 (2016) 390–397, https://doi.org/10.1016/j.ecoenv.2015.09.018.

[30] A. Shil, M. Saha, C. Debnath, S.A. Hussain, D. Bhattacharjee, Matrix dependent changes in metachromasy of crystal violet in Langmuir-Blodgett films, Chem. Phys. Lett. 665 (2016) 76–84, https://doi.org/10.1016/j.cplett.2016.10.027.

[31] P. Tang, A.Y. El-Moghazy, B. Ji, N. Nitin, G. Sun, Unique "posture" of rose Bengal for fabricating personal protective equipment with enhanced daylight-induced biocidal efficiency, Mater. Adv. 2 (2021) 3569–3578, https://doi.org/10.1039/D1MA00100K.

[32] Y. Xiong, J. Chen, M. Duan, S. Fang, Real-time measurement of the crystal violet adsorption behavior and interaction process at the silica-aqueous interface by near-field evanescent wave, Chem. Chem. Phys. 20 (2018) 19208–19220, https://doi.org/10.1039/C8CP03552K.

[33] A.W.H. Lee, B.K. Pilapil, H.W. Ng, B.D. Gates, Microwave assisted formation of monoreactive perfluoroalkylsilane-based self-assembled monolayers, Chem. Commun. 51 (2015) 2060–2063, https://doi.org/10.1039/C4CC07494G.

[34] N. Kashef, Y.Y. Huang, M.R. Hamblin, Advances in antimicrobial photodynamic inactivation at the nanoscale, Nanophotonics 6 (2017) 853–879, https://doi.org/10.1515/nanoph-2016-0189.

[35] K.J. Heo, S.B. Jeong, J. Shin, G.B. Hwang, H.S. Ko, Y. Kim, D.Y. Choi, J.H. Jung, Water-repellent TiO2-organic dye-based air filters for efficient visible-light-activated photochemical inactivation against bioaerosols, Nano Lett. 21 (4) (2021) 1576–1583, https://doi.org/10.1021/acs.nanolett.0c03173.

[36] N.M. Inada, H.H. Buzzá, K.C. Blanco, L.D. Dias (Eds.), Photodynamic Therapy - From Basic Science to Clinical Research. London, United Kingdom, IntechOpen (2021). https://doi.org/10.5772/intechopen.77705.

[37] D. Avnir, D. Levy, R. Reisfeld, The nature of the silica cage as reflected by spectral changes and enhanced photostability of trapped rhodamine 6G, J. Phys. Chem. 88 (1984) 5956–5959, https://doi.org/10.1021/j150668a042.

[38] N. Turgeon, M.-J. Toulouse, B. Martel, S. Moineau, C. Duchaine, M.V. Yates, Comparison of five bacteriophages as models for viral aerosol studies, Appl. Environ. Microbiol. 80 (14) (2014) 4242–4250, https://doi.org/10.1128/AEM.00767-14.

[39] G. Brankston, L. Gitterman, Z. Hirji, C. Lemieux, M. Gardam, Transmission of influenza A in human beings, Lancet Infect. Dis. 7 (2007) 257–265, https://doi.org/10.1016/S1473-3099(07)70029-4.

[40] H. Zhang, J. Liu, X. Zhang, C. Huang, Y. Zhang, Y. Fu, X. Jin, Design of three-dimensional gradient nonwoven composites with robust dust holding capacity for air filtration, J. Appl. Polym. Sci. 136 (2019) 1–9, https://doi.org/10.1002/app.47827.

[41] K.-K. Wang, S. Song, S.-J. Jung, J.-W. Hwang, M.-G. Kim, J.-H. Kim, J. Sung, J.-K. Lee, Y.-R. Kim, Lifetime and diffusion distance of singlet oxygen in air under everyday atmospheric conditions, Phys. Chem. Chem. Phys. 22 (38) (2020) 21664–21671, https://doi.org/10.1039/d0cp00739k.

[42] Y. Li, S. Yang, C. Sun, L. Wang, Q. Wang, Aqueous photofate of crystal violet under simulated and natural solar irradiation: Kinetics, products, and pathways, Water Res. 88 (2016) 173–183, https://doi.org/10.1016/j.watres.2015.10.007.

[43] M. Duan, J. Wu, Y. Xiong, S. Fang, J. Chen, Characterization and differentiation of the adsorption behavior of crystal violet and methylene blue at the silica/water interface using near field evanescent wave, Soft Matter 14 (36) (2018) 7516–7525, https://doi.org/10.1039/c8sm01385c.

[44] K. Belkassa, M. Khelifa, I. Batonneau-Gener, K. Marouf-Khelifa, A. Khelifa, Understanding of the mechanism of crystal violet adsorption on modified halloysite: Hydrophobicity, performance, and interaction, J. Hzard. Mater. 415 (2021) 125656, https://doi.org/10.1016/j.jhazmat.2021.

[45] C. Weyermann, D. Kirsch, C. Costa Vera, B. Spengler, Evaluation of the photodegradation of crystal violet upon light exposure by mass spectrometric and spectroscopic methods, J. Forensic Sci. 54 (2009) 339–345, https://doi.org/10.1111/j.1556-4029.2008.00975.x.

[46] L. Ayed, J. Cheriaa, N. Laadhari, A. Cheref, A. Bakhrouf, Biodegradation of crystal violet by an isolatedBacillus sp. Ann. Microbiol. 59 (2) (2009) 267–272, https://doi.org/10.1099/ijs.0.63567-0.

[47] Y. Bai, C.B. Han, C. He, G.Q. Gu, J.H. Nie, J.J. Shao, T.X. Xiao, C.R. Deng, Z.L. Wang, Washable multilayer triboelectric air filter for efficient particulate matter PM2.5 removal, Adv. Funct. Mater. 28 (2018) 1–8, https://doi.org/10.1002/adfm.201706680.

[48] S. Nie, Q. Fu, X. Lin, C. Zhang, Y. Lu, S. Wang, Enhanced performance of a cellulose nanofibrils-based triboelectric nanogenerator by tuning the surface polarizability and hydrophobicity, Chem. Eng. J. 404 (2021) 126512. doi: 10.1016/j.cej.2020.126512.

[49] A.F. Diaz, R.M. Felix-Navarro, A semi-quantitative tribo-electric series for polymeric materials: The influence of chemical structure and properties, J. Electrost. 62 (2004) 277–290, https://doi.org/10.1016/j.elstat.2004.05.005.